Published paper:

D. Žarko, M. Kovačić, S. Stipetić and D. Vuljaj, "Optimization of electric drives for traction applications," *2017 19th International Conference on Electrical Drives and Power Electronics (EDPE)*, Dubrovnik, 2017, pp. 15-32.

http://dx.doi.org/10.1109/EDPE.2017.8123278

Optimization of Electric Drives for Traction Applications

Damir Žarko, Marinko Kovačić, Stjepan Stipetić, Damir Vuljaj
University of Zagreb Faculty of Electrical Engineering and Computing
Department of Electrical Machines, Drives and Automation
Zagreb, Croatia
damir.zarko@fer.hr, marinko.kovacic@fer.hr, stjepan.stipetic@fer.hr, damir.vuljaj@fer.hr

Abstract—**The paper presents an overview of various steps required for solving the problem of designing electric drives for traction applications. The design problem is solved as an optimization problem with multiple objectives subject to various constraints governed by physical characteristics and limitations of materials and specific parts used for the assembly of electric motors and power converters, international standards, specific requirements of vehicle dynamics, available space, and cost. The drive components are optimized by modelling their interaction in the drive system. The principle is illustrated on an example of multiobjective Pareto optimization of a low floor tram using mixed integer distributed ant colony optimization.**

Keywords—electric traction; electric drive; multiobjective optimization; mixed integer distributed ant colony optimization; scaling laws; three-level converter; averaged model

I. INTRODUCTION

Electric traction drive in a modern electric vehicle is a complex system that is very carefully analyzed and optimally composed of components which interact synergistically. In order to achieve the optimal performance of the drive, it is important to make the design of the main drive components (electric motor, power converter, traction transformer and drive control system) inseparable from the design of the entire drive system. In this approach, it is required in the design stage to model in sufficient detail the required motion cycles of the vehicle and to simulate the electric drive system and its components to find the solution that will ensure the required performance. Parameters and characteristics of the electric drive components thus determined can be utilized as constraints for the component design. This is an iterative process which may have specific goals of optimizing the vehicle performance in terms of initial equipment cost, energy consumption during exploitation, or the Life Cycle Cost (LCC) of the vehicle. The LCC is very often a selected method for establishing the economic merit of a vehicle since it includes its initial cost, energy consumption during the period of exploitation and the cost of maintenance.

This paper shows the basic steps required for definition of the traction drive design problem followed by its mathematical optimization. It includes consideration of the vehicle dynamics, motor and power converter size and ratings, conformity with standards for electric drive equipment, selection of the design variables and physical insight into connection between design variables and performance of the drive as a whole.

On a practical example, the paper illustrates the process of multiobjective Pareto optimization of a traction drive for modern low floor city tram using mathematical model of a permanent magnet motor based on 2D maps of parameters calculated using finite element method (FEM) combined with geometric scaling, an analytical averaged model of neutral point clamped (NPC) three-level converter, and mixed integer distributed ant colony optimization (MIDACO) algorithm. The field oriented control with maximum torque per ampere (MTPA) and flux weakening (FW) at high speeds are assumed. Design trade-offs are considered between traction motor size and energy dissipated in a standard driving cycle of the tram.

II. MODELLING OF VEHICLE DYNAMICS

A. *Definition of vehicle performance*

The performance of a vehicle is usually described by its maximum cruising speed, gradeability, and acceleration [1]. In addition, the dynamics of road vehicles defined by time variation of speed in a predefined repetitive pattern may be designed to comply with some standard driving cycles (e.g. NEDC, FTP-75, WLTP, JC08, etc.). Those cycles are commonly used for tailpipe emission certification and fuel economy testing of passenger cars with internal combustion engines (ICE). In electric cars, they are used to assess the vehicle range and energy consumption (e.g. WLTP).

The desired maximum cruising speed determined by the equilibrium between the tractive effort of the vehicle and the resistance (rolling resistance and aerodynamic drag) on a flat road usually exceeds the maximum speed of driving cycles.

The speed variation is characterized by maximum acceleration a_{max} and maximum deceleration a_{kmax} on a flat road which, together with the mass of the vehicle and resistance, affect the maximum acceleration and braking force on the axle, i.e. the maximum required torque on the motor shaft. The maximum torque is also dependent on the gearbox and differential ratio. The maximum power which traction drive needs to develop depends on the minimum required acceleration time and maximum allowed braking distance assuming maximum speed of the vehicle and considering the mass of the vehicle and resistance. The maximum power can also depend on the desired maximum speed and the resistance force since the power required at that speed may exceed the maximum power defined by acceleration time.

In passenger vehicles on rails like electric trams and electric multiple units the maximum acceleration and deceleration rates are limited ($a_{max}/a_{kmax} \leq 1.1/1.3$ m/s^2) by the comfort of the passengers so that passengers who are standing during speed variations do not experience excessive inertial forces. During emergency braking maximum decelerations between 2 and 3 m/s^2 are allowed. In passenger electric cars, higher values of a_{max} and a_{kmax} are allowed depending on the vehicle type, energy consumption and comfort rate.

Gradeability is usually defined as the grade (or grade angle) that the vehicle can overcome at a certain constant speed [1]. On a flat road, it can represent the available tractive force at the given speed (v) for further acceleration.

Fig. 1 shows an example of maximum tractive effort curve of an electric vehicle together with resistance curves on different slopes and force vs. speed pairs (marked with ×) which belong to WLTP class 3 (Fig. 2) driving cycle on a flat road with resistance at zero slope considered. It should be noted that magnitudes of the negative forces are smaller than those of the positive forces due to braking effect of the resistance force, so the electric machine needs to develop smaller braking force than accelerating force to achieve the speed variation according to WLTP cycle.

Considering this example, the components of an optimized electric drive must be sized in electromagnetic, thermal and mechanical sense to withstand the repetitive pattern of the drive cycle continuously and can be optimized at the same time to achieve minimum energy consumption for the WLTP cycle thus providing maximum range. The maximum acceleration rate (or maximum slope) and maximum speed of standard driving cycles are in most cases smaller than the targeted maximum performance of commercial vehicles as indicated by the tractive effort envelope in Fig. 1 for which the maximum speed is 180 km/h, the maximum acceleration is 4 m/s^2, and the maximum slope is 25 %. For sizing the drive, it also important to estimate the duration of the peak performance points. It is not realistic to expect that the vehicle will continuously climb the maximum slope or drive at maximum cruising speed. For example, in the United States the minimum requirements for commercial vehicles used to be prescribed by the Code of Federal Regulations [2] which can be used as an orientation to set some constraints for sizing the drive components. The Code prescribes that the grade which the vehicle can start and climb for 20 s should be at least 20 % (11.5°), the grade which can be traversed up at 25 km/h should be at least 10 % (5.7°), and the speed which can be maintained for 5 minutes should be at least 75 km/h. With all these considerations, an example of a set of design constraints which can be used to determine the tractive effort and design electric drive components of an electric vehicle is:

- vehicle can achieve the speed/time profile of the WLTP Class 3 driving cycle in a continuous repetitive sequence,
- constant speed which must be maintained continuously is 130 km/h (motorway speed limit in many European countries),
- maximum cruising speed which can be maintained for 5 minutes is 180 km/h
- maximum acceleration/deceleration is 4 m/s^2
- maximum acceleration time to 100 km/h is 12 s,
- maximum stopping distance from 100 km/h to zero on a dry road when using regenerative braking alone is 105 m,
- the grade which the vehicle can start and climb for 20 s is at least 25 %.
- the vehicle needs to continuously maintain a minimum speed of 90 km/h up a 6 % grade,
- the grade which the vehicle can climb continuously at 40 km/h is at least 10 %.

These constraints have been used to obtain the plots in Fig. 1 for a vehicle+passenger mass of 1750 kg.

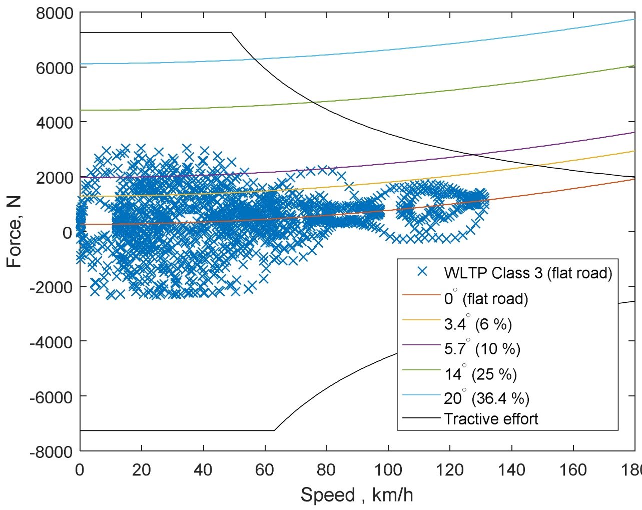

Fig. 1. Maximum tractive effort, resistance at different slopes, and tractive effort for WLTP Class 3 cycle of an electric vehicle powered by a single electric motor with single speed transmission

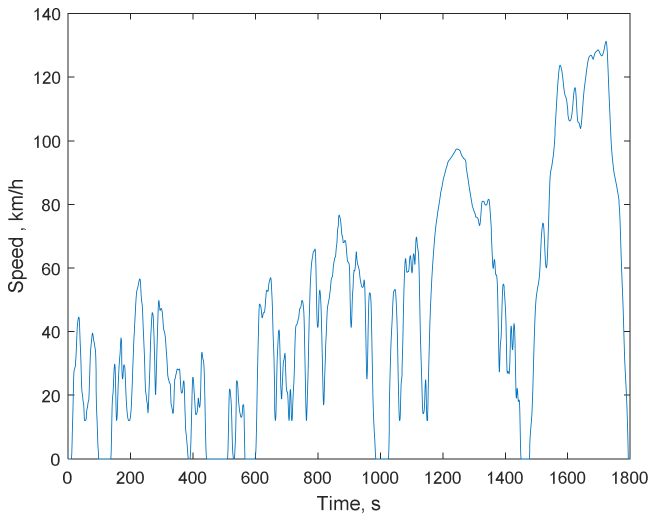

Fig. 2. Speed variation according to WLTP Class 3 driving cycle

B. *Calculation of vehicle dynamics*

The basic equation which describes the vehicle dynamics is

$$F = m_v a + F_{res} \tag{1}$$

where F is the total tractive effort, m_v is the mass of the vehicle including inertias of rotating components converted into translational mass, a is the acceleration and F_{res} is the total resistance. The resistance force includes rolling resistance (F_r), bearing friction ($F_{\mu b}$), aerodynamic drag (F_w), grading resistance (F_g), and resistance due to curves (F_c) appearing in railway traction in the case of fixed wheels on the common axle. Various analytical and semi-empirical expressions for calculation of resistance force components can be found in literature [1], [3], [4].

To calculate the maximum tractive effort envelope, the motion equation needs to be solved within the total length of the assumed vehicle path (s_d). A simple method based on discrete integration [5] can be used, whereby the path is divided into segments Δs of small length (about 1 m or less). It is assumed that the traction force within the segment Δs is constant. Based on the maximum acceleration and deceleration data, the maximum traction and braking force must be calculated and it must be verified that those forces are attainable considering the minimum force of adhesion. If the adhesion force is lower, correction of the input data needs to be made and the acceleration and/or deceleration requirements reduced. It is necessary to assume the initial values of the maximum power during acceleration (P_{max}) and maximum power during braking (P_{kmax}) which are entered into the calculation. If at the end of the calculation the acceleration time is longer than the default value, it is necessary to increase P_{max} and repeat the calculation. If the acceleration time is too short, the power P_{max} must be reduced. If the braking path (s_b) is calculated longer than the default, it is necessary to increase the power P_{kmax} or reduce its value if the braking path is shorter than the default.

The speed vector $v(s)$ is calculated for each segment Δs based on the equation

$$\left[v(s)\right]^2 - \left[v(s-\Delta s)\right]^2 = 2a\Delta s \tag{2}$$

where $v(s-\Delta s)$ is the initial speed at the beginning of the segment, and $v(s)$ is the speed at the end of the segment. Combining (1) and (2) yields the following algorithm.

a) *Acceleration*

$$v(s) = \sqrt{2\frac{F\left[v(s-\Delta s)\right] - F_{res}\left[v(s-\Delta s)\right]}{m_v}\Delta s + \left[v(s-\Delta s)\right]^2} \tag{3}$$

The calculation should start with the following values: s=0, $v(0)$=0, $F(0)$=F_{max}. If resistance at zero speed on a flat road is neglected, then F_{max}=$m_v a_{max}$. For each next step, new values of traction force, resistance force, acceleration and time should be defined as follows:

$$\begin{gathered} v(s) \rightarrow F_{res}\left[v(s)\right] \text{ (using formulas from literature)} \\ \text{if } F\left[v(s-\Delta s)\right]\left[v(s)\right] < P_{max} \Rightarrow F\left[v(s)\right] = F_{max} \\ \text{if } F\left[v(s-\Delta s)\right]\left[v(s)\right] \geq P_{max} \Rightarrow F\left[v(s)\right] = \frac{P_{max}}{v(s)} \\ a(s) = \frac{v(s) - v(s-\Delta s)}{t(s) - t(s-\Delta s)} \\ t(s) = t(s-\Delta s) + \frac{2\Delta s}{v(s) + v(s-\Delta s)} \end{gathered} \tag{4}$$

The acceleration ends when $v(s)$>v_{max}, where v_{max} is the maximum cruising speed.

b) *Driving at constant speed*

In this case, the traction force is equal to the force of the driving resistance. The speed $v(s)$, the resistance $F_{res}[v(s)]$, the acceleration $a(s)$ and the time $t(s)$ are calculated as in the case of acceleration, while $F[v(s)]$= $F_{res}[v(s)]$.

b) *Braking*

Braking begins when s_d-(s-Δs)≤s_b. This condition needs to be checked at the beginning of the calculation for each new segment of the route. Equation (3) is solved to obtain $v(s)$. For each next step

$$\begin{gathered} v(s) \rightarrow F_{res}\left[v(s)\right] \text{ (using formulas from literature)} \\ \text{if } \left|F\left[v(s-\Delta s)\right]\right|\left[v(s)\right] < F_{k\max} v(s) \Rightarrow F\left[v(s)\right] = -\frac{P_{k\max}}{v(s)} \\ \text{if } \left|F\left[v(s-\Delta s)\right]\right|\left[v(s)\right] \geq F_{k\max} v(s) \Rightarrow F\left[v(s)\right] = -F_{k\max} \\ a(s) = \frac{v(s) - v(s-\Delta s)}{t(s) - t(s-\Delta s)} \\ t(s) = t(s-\Delta s) + \frac{2\Delta s}{v(s) + v(s-\Delta s)} \end{gathered} \tag{5}$$

In the given expressions, the variables F_{kmax} and P_{kmax} have a positive value. Force F has a negative value. If resistance at zero speed on a flat road is neglected, then F_{kmax}=$m_v a_{kmax}$. The calculation ends when s≥s_d. If the speed at the end of the path is higher than zero, it is necessary to increase P_{kmax} and repeat the calculation. If the speed has dropped to zero before the end of the path, it is necessary to reduce the P_{kmax}. The procedure is repeated until the speed is equal to zero at the end of the path.

This algorithm has been used to calculate the maximum tractive effort envelope shown in Fig. 1 using numerical values of design data and constraints listed in Section IIA.

III. Sizing of the Traction Drive

A. *Consideration of motor and power converter size and ratings*

The duration of specific load points is important because the size of the electric motor is not only a function of instantaneous torque, but also depends on the duration of the load, its magnitude, cooling type (e.g. fan cooled or liquid cooled) and degree of mechanical protection (e.g. totally enclosed or open), which all affect the time variation and the maximum value of the winding temperature. Since the motor is mostly made of iron and copper of a certain volume, it has a certain thermal capacitance so its temperature will not change instantaneously. Since thermal time constants are measured in minutes, the motor can withstand short term overloads (e.g. torque corresponding to the maximum tractive effort) without overheating beyond the maximum allowed temperature of its winding insulation thermal class (e.g. F or H) and therefore can be sized to a smaller volume than required for developing the peak torque continuously. In permanent magnet motors, the temperature variation of the magnets must be monitored as well not to exceed the value above which the magnet will demagnetize (Curie temperature) or the value at which the operating point of the magnet will approach the knee of its B-H curve closer than some allowed margin (e.g. 0.2 T [6]).

A simple approach to motor sizing can be based on averaging of losses in the motor and its speed during a driving cycle which can be used to calculate the electric current and torque which, combined with the average speed, yield the thermal equivalence of rated torque and power for continuous duty (IEC S1 duty cycle). Therefore, the motor designed based on equivalent S1 ratings should be able to thermally satisfy the requirements of the drive cycle dynamics. Such example is shown in [7] where steady state winding temperature of an interior permanent magnet (IPM) motor for electric tram calculated from thermal model using equivalent ratings for continuous duty was very close to the average value of the winding temperature variation obtained from transient thermal simulation of the actual driving cycle load. This approach works well if motor sizing is based solely on the driving cycle requirement. In electric cars, there are additional peak performance points as explained earlier, which put additional thermal stress on the machine and may require the usage of transient thermal models for motor sizing.

The sizing of the power switches requires a different approach when considering thermal stress. Unlike the motors, the thermal capacitance of a power switch (e.g. IGBT transistor) in the power converter is negligible (0.1-10 s to reach maximum permissible temperature) so its current rating must be chosen according to the maximum instantaneous load of the motor. Typical rated collector-emitter voltages for IGBTs commonly used in power applications are 600 V, 650 V, 900 V, 1200 V, 1700 V, 2500 V, 3300 V, 4500 V, 6500 V. The rated rms line voltages applied to electric drive motors should be around 2.5 times smaller than ratings of IGBTs to account for transient voltages which add to the normal DC bus voltage due to voltages induced across parasitic inductances [8]. It makes sense to select the rated voltage of the traction motor according to the rating of the IGBT device to fully utilize its voltage capacity thus reducing the required current rating of the device for the given kVA rating of the traction drive. Therefore, if rated voltage of the motor is one of design variables, it should be varied in discrete steps according to the standard voltage ratings of IGBTs.

The rating of the DC bus is dependent on the power supply. For example, for railway applications in the case of KONČAR EMU the AC voltage is 25 kV followed by a traction transformer 25/0.8 kV, the DC bus is rated 1500 V, the IGBT switches are rated 3300 V and the motor is rated 1000 V. In the case of an electric tram KONČAR TMK2200 the DC bus voltage is rated 600 V (+20% - 30%), the IGBT switches are rated 1700 V, and the motor is rated 400 V. For most commercial passenger electric vehicles, the battery pack, and hence the DC bus voltage, is rated between 300 V and 400 V. The German Electrical and Electronic Manufacturers' Association prescribes the DC bus voltage rating for electric vehicles to 400 V, the power switch rating to 650 V, and the AC motor voltage to 300 V [9].

B. Design variables for traction motor and power converter

The traction motor and power converter are defined by their design variables which affect their size and performance. In the case of motor there is a set of variables which define its geometry (e.g. number of slots and poles, slot and permanent magnet shape and size, air gap length, stack length, stator and rotor diameters, number of conductors per slot, etc.) and the variables which define materials and electromagnetic constraints (core material, permanent magnet material, current density, maximum flux densities in the teeth and yoke, minimum efficiency, maximum winding and magnet temperature, etc.). The influence of those variables on motor performance is evaluated in the design stage by using reasonably accurate and computationally inexpensive models. In the case of induction motors, analytical models can be solved quickly and provide acceptable results. For PM motors with surface mounted magnets (SPM), various analytical models exist (e.g. models based on conformal mapping [10], [11], mode matching technique [12], [13], harmonic modelling [14], magnetic equivalent circuits [15], [16]) with fairly high accuracy, especially if saturation can be neglected which is often the case when magnets are sufficiently thick resulting in a large physical air gap. In the case of IPM motors, analytical models are inaccurate due to significant influence of saturation of thin bridges separating rotor surface from the cavities in the rotor yoke which hold the magnets. In that case finite element method (FEM) is the only reliable option, but its problem is long computational time. An alternative is to use a model based on d and q axis flux maps calculated using FEM as a function of d and q axis currents ($\psi_d = f(i_d, i_q)$, $\psi_q = f(i_d, i_q)$) [17] in combination with scaling laws [18]. For modelling of dynamic performance, the variation of flux linkages on angular position of the rotor can be added as well [19]. This type of model is applicable to both SPM and IPM motors, it considers saturation in the motor, and is computationally very efficient. It relies on a detailed design of a so-called referent motor which should be sized close enough for the demands of the vehicle dynamics. Further tuning of the design is performed by scaling of its geometry using only three parameters, the factors of radial scaling k_R, axial scaling k_A, and rewinding k_w. The rewinding factor assumes changing the ratio of the number of turns per coil (N_c) to the number of parallel paths (a_p) to match the terminal voltage of the motor. The higher number of turns per coil increases the field weakening range, reduces the speed at which the motor reaches its rated voltage and reduces the current required by the inverter to develop the starting torque. However, there is a trade-off here because higher number of turns leads to lower winding losses and higher core losses. Since winding losses are usually dominant over core losses, there is an optimal combination of N_c and a_p which minimizes the motor losses when acceleration from zero to maximum speed is considered using maximum tractive effort. From the inverter point of view, the minimum current is always desirable since it minimizes the conduction and switching losses for the given switching frequency.

The described influence of winding parameters can be demonstrated on the example of an IPM motor modelled in per unit system assuming MTPA control. Let the number of turns per coil (N_{c0}) and the number of parallel paths (a_{p0}) of the referent motor be tuned so that motor reaches its rated voltage U_n at the corner speed ω_c. The corner speed is the speed at which tractive effort envelope ends the constant maximum torque region and starts the constant power region. The base voltage and speed for per unit system are set to U_n (phase voltage) and ω_c, and the base current is the current I_{n0} for which the referent motor requires rated voltage at corner speed assuming MTPA control.

The per unit d and q inductances of the referent motor can be marked as L_{d0} and L_{q0}, the permanent magnet flux linkage is ψ_{md0} and the current at maximum starting torque is $I_{T\max0}$. Rewinding assumes the same current density in the conductors so the total ampere-turns per slot will not change with k_W for the same amount of torque the motor develops at a certain speed. The factor k_W is given by

$$k_W = \frac{N_c/a_p}{N_{c0}/a_{p0}} \tag{6}$$

and the parameters of the rewound motor are then

$$\begin{aligned} &L_d = k_W^2 L_{d0}, \quad L_q = k_W^2 L_{q0} \\ &\psi_{md} = k_W \psi_{md0} \\ &I_{T\max} = \frac{1}{k_W} I_{T\max 0} \end{aligned} \tag{7}$$

The rated voltage equals U_n for both the referent and the rewound motor because it is defined by the available DC bus voltage level. The stator resistance is neglected and there are only two parameters which define the referent motor, saliency ratio and characteristic current, given by

$$\begin{aligned} &\xi = \frac{L_q}{L_d} = \frac{k_W^2 L_{q0}}{k_W^2 L_{d0}} = \frac{L_{q0}}{L_{d0}} \\ &I_{c,pu} = \frac{\psi_{md}}{L_d I_n} = \frac{k_W \psi_{md0}}{k_W^2 L_{d0} \dfrac{I_{n0}}{k_W}} = \frac{\psi_{md0}}{L_{d0} I_{n0}} \end{aligned} \tag{8}$$

which are unaffected by rewinding of the motor. The selected values are ξ=3, I_c=1.2. The parameters of the referent motor in per unit system are then calculated from

$$\gamma_n = a\sin\left[\frac{-I_c + \sqrt{I_c^2 + 8 I_{n0}^2 (\xi - 1)^2}}{4 I_{n0}(1-\xi)}\right] \tag{9}$$

$$\begin{aligned} &L_{d0} = \frac{U_n}{\omega_c \sqrt{(I_{n0}\sin\gamma_n)^2 + \xi^2 (I_{n0}\cos\gamma_n)^2}}, \quad L_{q0} = \xi L_{d0} \\ &\psi_{md0} = L_{d0} I_c \end{aligned} \tag{10}$$

where γ_n is the optimal angle of the current vector (placed in the 2nd quadrant) with respect to the q axis of the synchronously rotating d-q reference frame which yields MTPA control, and I_{n0}=1 pu, ω_c=1 pu. The per unit torque and voltage equations for any value of per unit current are given by

$$T = L_d \left[I_c I \cos\gamma + \frac{1}{2} I^2 (1-\xi)\sin(2\gamma) \right] \tag{11}$$

$$\begin{aligned} &U = \sqrt{U_d^2 + U_q^2} \\ &U_d = -\omega L_q I_q = -\omega L_q I \cos\gamma \\ &U_q = \omega(L_d I_d + \psi_{md}) = \omega(L_d I \sin\gamma + \psi_{md}) \\ &U = \omega\psi \end{aligned} \tag{12}$$

where ω is the per unit value of the angular frequency (ω=1 pu at corner speed), γ is the optimal angle of the current vector according to MTPA control, and ψ is the per unit flux linkage. In the field weakening the angle γ is adjusted to minimize the stator current and satisfy the voltage constraint ($U \le U_n$). The factor k_W is varied from 1 to 0.6 and (6) to (10) are used to calculate the variation of motor voltage and current for different values of k_W during acceleration of the vehicle from standstill to maximum speed of 4 pu. The results are shown in Fig. 3. It can be noticed that with reduction of the number of turns the current for the starting torque increases and the speed at which the rated voltage is reached also increases.

The air gap flux Φ is related to the flux linkage ψ according to $\Phi = N_s \psi$, where N_s is the total number of turns connected in series per phase. Since N_s is also scaled by k_W, it follows that

$$\Phi_{pu} = \frac{\Phi}{\Phi_0} = \frac{\psi}{N_s}\frac{N_{s0}}{\psi_0} = \frac{\psi_{pu}}{k_W} \tag{13}$$

where ψ_0, Φ_0 and N_{s0} are the flux linkage, air gap flux and the number of turns connected in series of the referent motor respectively. The variation of ψ and Φ with speed is plotted in Fig. 4. As expected, in the constant torque region the flux Φ is not affected by rewinding. However, in the flux weakening region the motor with higher number of turns (higher k_W) will have its flux weakened at lower speed. Since flux densities in the parts of the magnetic circuit of the motor are approximately proportional to the air gap flux, and if it is assumed that total core losses (hysteresis+eddy current) are roughly proportional to the multiple of squared values of flux density and frequency raised to the power of 1.8 ($P_{Fe} \sim B^2 f^{1.8} \sim \Phi^2 \omega^{1.8}$), then air gap flux vs. speed plots in Fig. 4 can be easily converted to core loss plots shown in Fig. 5 which compare how core losses vary with speed and the number of turns relative to the core losses of the referent motor.

The motor torque is a function of air gap flux density and total ampere turns in the slots. Since motor always needs to develop the same values of torque defined by vehicle dynamics, in the constant torque region the air gap flux density is constant and hence the ampere turns per slot are also constant. Therefore,

$$AT = JS_{slot}f_{fill} = J_0 S_{slot} f_{fill} = AT_0 \tag{14}$$

where J is the current density, S_{slot} is the cross-sectional area of the slot, and f_{fill} is the slot fill factor (ratio of copper to slot area, presumably unaffected by rewinding). The values with subscript 0 refer to the referent motor. Equation (14) is valid only if J=J_0, which means that current density in the constant torque region is unaffected by rewinding. The per unit value of current density is given by

$$J_{pu}(\omega) = \frac{J(\omega)}{J_{n0}} = \frac{\dfrac{I(\omega) z_{slot}}{a_p S_{slot} f_{fill}}}{\dfrac{I_{n0} z_{slot0}}{a_{p0} S_{slot} f_{fill}}} = I_{pu}(\omega) k_W \tag{15}$$

where J_{n0} is the current density of the referent motor corresponding to the phase current I_{n0}, z_{slot} and z_{slot0} are the number of conductors per slot of the rewound and referent motor. The winding losses are proportional to the current density squared regardless of the number of turns if f_{fill} is constant, so variation of the winding losses relative to the winding losses of the referent motor can be obtained from the current plots in Fig. 3 using the squared value of current density from (15). The winding losses are plotted together with the core losses in Fig. 5. It can be noticed that all winding configurations have the same winding and core losses in the constant torque region. Above corner speed the winding losses are reduced as the rewinding factor reduces (i.e. N_c/a_p reduces), while iron losses are increased. The total energy consumed by the motor during acceleration will reach a minimum value for some k_W for which the sum of time integrals of P_{Cu} and P_{Fe} is minimal. This minimum depends on the distribution of core and winding losses in the referent motor, i.e. on their ratio P_{Fe0}/P_{Cu0}.

Unlike traction motors, semiconductor devices are not custom designed to match the required motor current and voltage. Manufacturers provide devices according to voltage and current ratings in some discrete sets of values, so for designing the traction drive, they should be picked from a catalogue and then modelled and analyzed using the data provided by manufacturer's datasheets. For traction drive optimization, a database of devices should be built which are then selected based on input voltage and current rating. The criterion for selection of a device from a group which satisfies the voltage and current constraints can be its cost or total losses accumulated during a driving cycle. The cost increases with higher voltage and current while power losses are related to motor current and inherent properties of the device. The power losses in the voltage source inverter (VSI) consist of conduction and switching losses in the IGBTs and diodes. The losses depend on the motor current, switching frequency, modulation type and properties of the semiconductor devices. The very basic model for calculation of VSI losses assuming carrier based sinusoidal pulse width modulation (PWM) can be presented in the form of 2nd order polynomial as a function of current

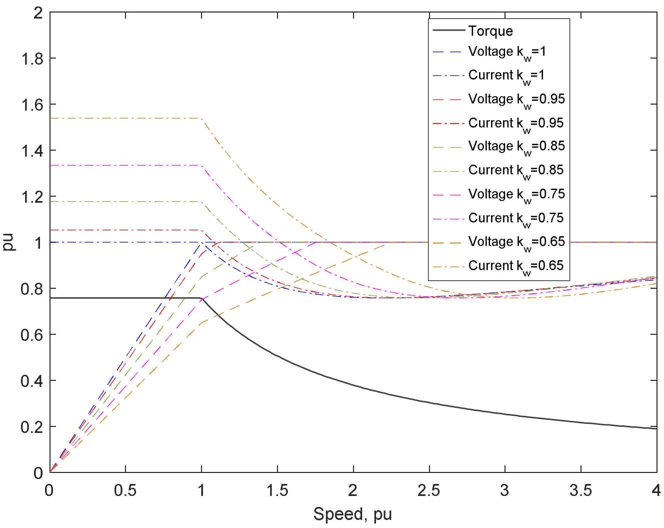

Fig. 3. Variation of motor voltage and current as a function of speed for different values of the rewinding factor

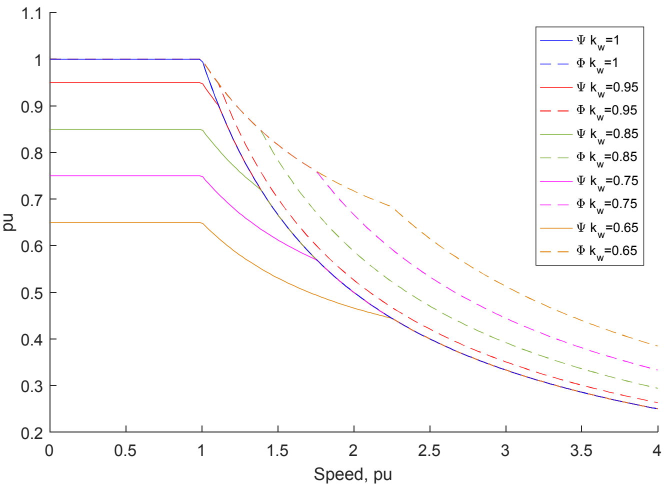

Fig. 4. Variation of flux linkage ψ and air gap flux Φ as a function of speed for different values of the rewinding factor

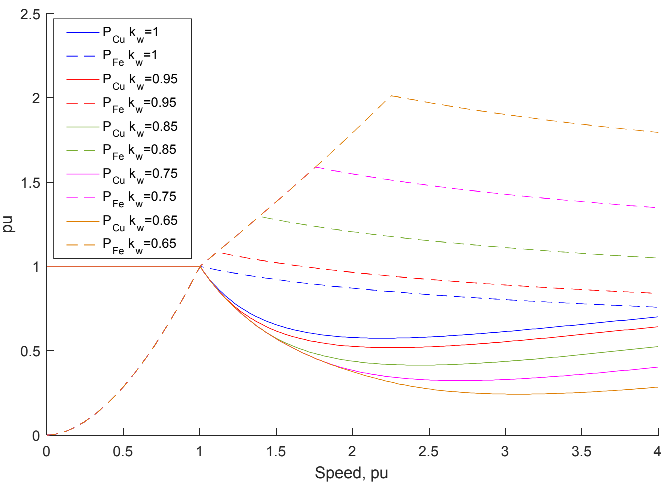

Fig. 5. Variation of per unit winding and core losses as a function of speed for different values of the rewinding factor

$$P_{VSI} = k_{sl} I + k_{cl1} I + k_{cl2} I^2 \tag{16}$$

where k_{sl} is the coefficient of switching losses, k_{cl1} and k_{cl2} are the coefficients of conduction losses. The coefficient k_{cl1} considers the knee voltages of the IGBT and diode and k_{cl2} considers the resistances of the linearized output characteristics of the devices. For sinusoidal PWM it is reasonable to assume that 65 % of total losses at rated current I_{n0} will be switching losses, and 70 % of conduction losses are attributable to resistance losses. If total normalized VSI losses in the referent motor are 1 pu, then k_{sl}=0.65, k_{cl1}=0.105 and k_{cl2}=0.245. Combining these coefficients with current variations in Fig. 3 and (16) yields the VSI losses of the rewound motors relative to the losses of the referent motor shown in Fig. 6. It is obvious that k_W=1 yields minimum losses of the VSI, but this not necessarily the optimal choice when motor and VSI losses are added together and the total energy dissipation during a driving cycle is calculated. This choice depends on the share of individual power losses at particular load and speed.

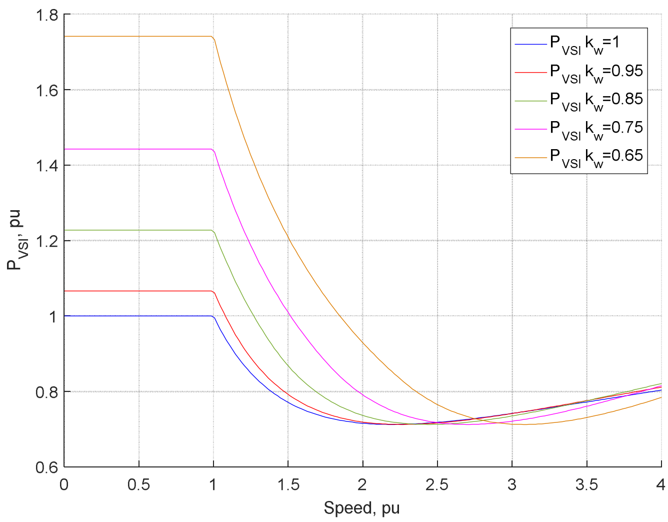

Fig. 6. Variation of VSI losses as a function of speed for different values of the rewinding factor

IV. Traction Drive Optimization

Product development always involves certain design methods that seek solutions that would be more favourable for both the manufacturer and the end user, mainly for better market placement. This concept of thinking has led to the development of numerous optimization methods, such as deterministic methods that guarantee the optimum solution as well as metaheuristic algorithms that do not guarantee optimum but are capable of handling very complicated optimization tasks. The downside of deterministic algorithms is the requirement of a strict mathematical definition of a problem which is often not feasible nor natural.

Metaheuristic algorithms are approximate and usually non-deterministic whose goal is to efficiently explore the search space in order to find near-optimal solutions. They are based on natural processes that take place daily (evolution, ant colony, bee swarm...). This similarity is not surprising since natural processes in some way optimize the world around us.

Multiobjective optimization implies finding an optimal solution involving more than one objective function to be optimized simultaneously. The idea is to evaluate all the objective functions simultaneously and use nondominated selection to find a population of solutions which belong to the Pareto optimal set. A vector of decision variables is Pareto optimal if there exists no other feasible vector from the feasible region of the problem (i.e. where the constraints are satisfied) which would decrease some objectives without causing a simultaneous increase in at least one other objective [20]. The decision maker (e.g. traction drive designer) then chooses a single solution from the Pareto set as the compromise which suits his/her objectives the best.

The problem of traction drive optimization belongs to the class of *mixed integer nonlinear programming* (MINLP) [21] and includes nonlinear functions and discrete variables. The multiobjective MINLP problem can be formulated as

$$\begin{aligned}
&\text{Minimize } f_j(\mathbf{x},\mathbf{y}) \;\; (\mathbf{x} \in \mathbb{R}^{n_{con}}, \mathbf{y} \in \mathbb{N}^{n_{\text{int}}}, n_{con}, n_{\text{int}} \in \mathbb{N},\\
&\qquad\qquad j = 1,\ldots,M \in \mathbb{N})\\
&\text{where} \quad g_i(\mathbf{x},\mathbf{y}) = 0, \;\; i = 1,\ldots,m_{eq} \in \mathbb{N}\\
&\qquad\qquad g_i(\mathbf{x},\mathbf{y}) < 0, \;\; i = m_{eq}+1,\ldots,m \in \mathbb{N}\\
&\qquad\qquad \mathbf{x}_L \le \mathbf{x} \le \mathbf{x}_U \quad (\mathbf{x}_L, \mathbf{x}_U \in \mathbb{R}^{n_{con}})\\
&\qquad\qquad \mathbf{y}_L \le \mathbf{y} \le \mathbf{y}_U \quad (\mathbf{y}_L, \mathbf{y}_U \in \mathbb{N}^{n_{\text{int}}})
\end{aligned} \tag{17}$$

In this formulation $f_j(\mathbf{x},\mathbf{y})$ is one of the M objective functions to be minimized which depends on $\mathbf{x}$, the vector of n_{con} continuous variables and $\mathbf{y}$, the vector of n_{int} discrete variables. Functions $g_1(\mathbf{x},\mathbf{y}),\ldots,g_{meq}(\mathbf{x},\mathbf{y})$ are equality constraints while functions $g_{meq+1}(\mathbf{x},\mathbf{y}),\ldots,g_m(\mathbf{x},\mathbf{y})$ are inequality constraints. The lower and upper limits of variables $\mathbf{x}$ and $\mathbf{y}$ are marked with $\boldsymbol{x}_L$, $\boldsymbol{x}_U$ and $\boldsymbol{y}_L$, $\boldsymbol{y}_U$.

The multiobjective traction drive optimization will be demonstrated on an example of the low floor tram KONČAR TMK2200. This actual tram is driven by six induction motors powered by three 2-level inverters. In this study an alternative drive will be considered consisting of four IPM motors powered by four neutral point clamped three-level converters.

The drive optimization of an electric tram is by nature a MINLP type of multiobjective design problem. The models of drive components (motor, VSI) are nonlinear (e.g. FEM based motor model), some variables are continuous (e.g. motor stack length and outer diameter) and some are discrete (e.g. motor core or permanent magnet material, number of winding turns, VSI power modules). The multiobjective nature can be illustrated in the following manner: If the most energy efficient vehicle is to be considered, the result of the optimization process will be oversized motor and power converter that will increase the purchase price. On the other hand, if the production price is set as the only objective function, the optimization could result in a product with poor energy efficiency. The customer and the manufacturer are often interested in the relationship between these two competing objectives which facilitates their final design choice.

It has already been mentioned in Chapter III that models of the motor and inverter need to be accurate and computationally efficient since they need to be utilized many times during optimization process. The description of such models used for optimization of the tram drive follows in the next two sections.

A. Model of the IPM traction motor for the low floor tram

For modelling the IPM motor in the driving cycle of the tram it is assumed that dynamics of the current control loop is much faster than dynamics of the speed loop, so the voltages, currents, torque and speed can be calculated as a sequence of steady state operating points at discrete time instants. The steady state model of the IPM motor is defined in the rotating *d-q* reference frame with equations

$$
\begin{aligned}
&U_d = R_s I_d - \omega_s \Psi_q \\
&U_{qs} = R_s I_q + \omega_s \Psi_d \\
&\Psi_q = \Psi_{mq} + L_q I_q + L_{qd} I_d \\
&\Psi_d = \Psi_{md} + L_d I_d + L_{dq} I_q \\
&U_d = R_s I_d - \underbrace{\omega_s \Psi_{mq}}_{E_q} - \underbrace{\omega_s L_q}_{X_q} I_q - \underbrace{\omega_s L_{qd}}_{X_{qd}} I_d \\
&U_q = R_s I_q + \underbrace{\omega_s \Psi_{md}}_{E_d} + \underbrace{\omega_s L_d}_{X_d} I_d + \underbrace{\omega_s L_{dq}}_{X_{dq}} I_q \\
&T_{em} = \frac{3}{2} p \Big[\Psi_{md} I_q - \Psi^r_{mq} I_d + \left(L_d - L_q\right) I_d I_q + \\
&\qquad L_{dq}\left(\left(I_q\right)^2 - \left(I_d\right)^2\right)\Big]
\end{aligned} \tag{18}
$$

where L_{dq} i L_{qd} are the cross-saturation inductances, Ψ^r_{md} and Ψ^r_{mq} are the *d* and *q* components of permanent magnet flux linkage, E_d and E_q are the induced voltages, T_{em} is the electromagnetic torque, and ω_s is the angular frequency ($2\pi f$). The following equality is also valid: $L_{dq} = L_{qd}$. The inductances and flux linkages in (18) are current dependent due to nonlinearity of the magnetic circuit caused by saturation.

The referent machine that will be rescaled in the optimization process is the IPM motor prototype (Fig. 7) designed and tested to achieve 50 % higher torque and power rating than existing induction motors of TMK2200 thus allowing the tram to be driven by four instead of six motors. More details on this motor can be found in [7] and [22].

The motor ratings for the equivalent continuous duty are given in Table I. This motor was designed for maximum torque density, but it was not sized to take into account the combined functioning of the entire system (motor+power converter). Therefore, the multiobjective optimization of the entire drive may yield an optimal Pareto set with different motor sizes depending on trade-off between the motor size and the total power losses within the driving cycle of the tram.

The model of the motor is obtained by creating 2D maps of inductances, PM flux linkage and torque in (18) calculated by magnetostatic FEM simulations at a fixed rotor position for the phase currents defined by the pairs of values of I_d and I_q.

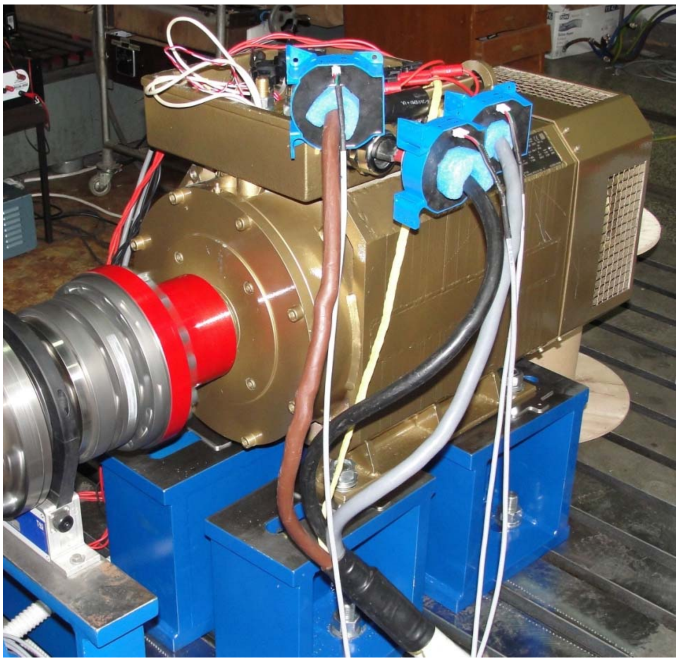

Fig. 7. Prototype of the IPM motor for the tram TMK2200 during testing

TABLE I. MEASURED RATINGS OF THE IPM MOTOR FOR CONTINUOUS DUTY

Rated shaft torque, Nm	475
Rated speed, min^{-1}	2380
Rated voltage (true rms), V	366.8
Rated current (true rms), A	221.6
Electric power input, kW	122.5
Shaft power, kW	118.4
Efficiency, %	96.67
Total losses, W	4100
Copper losses, W	1440
Iron losses, W	2318
Magnet losses (calculated), W	67
Friction and windage losses (calculated), W	275
Average winding temperature, °C	144.4
Average magnet temperature, °C	142.7

Since the referent motor will be continuously rewound during optimization process, the mapping of its parameters is performed assuming one turn per coil (N_{c0}=1) and no parallel paths (a_{p0}=1). With the assumption of sinusoidal current with peak value I_{0max}, the mapping is performed by defining the rectangular grid of currents in the 2nd (motoring) and 3rd (generating) quadrants of the *d-q* reference frame where the pairs of values (I_{d0}, I_{q0}) are defined in the intervals $-I_{0max} \leq I_{d0max} < 0$, $-I_{0max} \leq I_{q0max} < -I_{0max}$ in the steps of $\Delta I = I_{0max}/20$. The maximum rms current density in the map is set to J_m=12 A/mm^2 according to which the peak value of the current is calculated using

$$I_{0\max} = \sqrt{2} J_m S_{slot} f_{fill} \tag{19}$$

The total of 21×42=882 magnetostatic FEM simulations were carried out from which winding inductances, PM flux linkage and core losses were calculated using the method of permeance freezing [23].

The core losses are calculated from time variation of flux density at various locations along the height of the tooth and across the surface of the yoke. Since magnetostatic simulations are used for mapping the motor, the rotor motion is simulated by calculating the flux density values at a number of geometric points on the cross section of the tooth and yoke within the referent slot pitch and exactly the same points in every other consecutive slot pitch. Considering the fact that points in the referent slot pitch will have the same flux density values as the spatially shifted points in the consecutive slot pitches, but at different time instances due to rotor shift, the spatial distribution of flux density can be easily converted into its time variation in the referent slot pitch. The number of points (time instances) in a time waveform of flux density thus calculated equals the number of slot pitches per one repetitive winding pattern.

The Steinmetz formula in the form

$$P_{Fe} = \underbrace{k_h f B^{a+b\cdot B}}_{\text{hysteresis losses}} + \underbrace{k_e 2\pi^2 f^2 B^2}_{\text{eddy current losses}},\ \text{W/kg} \tag{20}$$

is used to calculate the losses where coefficients k_h, k_e, a and b are determined by curve fitting the losses of the material SURA M250-50 A from the catalogue at various frequencies and flux densities. For the purpose of motor modeling the losses are normalized by excluding the frequency from (20) and expressed as a sum of losses for each harmonic component of flux density in the teeth and yoke in each direction (radial and tangential)

$$P_{Fe0h} = X_{Fe}\sum_{\nu=1}^{\nu_{\max}} k_h \nu B_{yr\nu}{}^{a+b\cdot B_{yr\nu}} + k_h \nu B_{yt\nu}{}^{a+b\cdot B_{yt\nu}} + k_h \nu B_{tr\nu}{}^{a+b\cdot B_{tr\nu}}$$

$$P_{Fe0e} = X_{Fe}\sum_{\nu=1}^{\nu_{\max}} k_e 2\pi^2 \nu^2 B_{yr\nu}{}^2 + k_e 2\pi^2 \nu^2 B_{yt\nu}{}^2 + k_e 2\pi^2 \nu^2 B_{tr\nu}{}^{a+b\cdot B_{tr\nu}} \tag{21}$$

where X_{Fe} is the loss increase factor due to laser cutting and mechanical stress during core assembly (X_{Fe}=1.7), $\nu_{\max}$ is the maximum harmonic order attainable from the discrete time waveform, B_{yr} and B_{yt} are the stator yoke radial and tangential flux density components, and B_{tr} is the radial component of tooth flux density. The tangential component of flux density in the tooth is negligible. The total normalized losses P_{Fe0h} and P_{Fe0e} in the stator core are obtained by adding the losses in all geometric evaluation points assuming that flux density is constant in the incremental volume of a simple rectangular mesh surrounding each point. The total stator core losses are then

$$P_{Fe} = f P_{Fe0h} + f^2 P_{Fe0e} \tag{22}$$

where f is the frequency calculated from the rotor speed defined by the vehicle kinematics. The rotor core and magnet losses are neglected. The core losses in the rotor are located on the surface and cannot be calculated using the described method, while losses in the magnets are negligible because they are buried in the cavities far enough from the rotor surface.

The redesign of the referent motor is performed using scaling laws which include radial scaling of all dimensions in the cross section by the factor of k_R, axial scaling of the lamination stack by the factor of k_A and rewinding by the factor of k_W. This principle of scaling assumes that flux densities of the referent and scaled motor are equal which is satisfied by default in the case of axial scaling and rewinding. In the case of radial scaling this condition will be satisfied if the current density in the scaled motor is altered according to

$$J = \frac{1}{k_R} J_0 \tag{23}$$

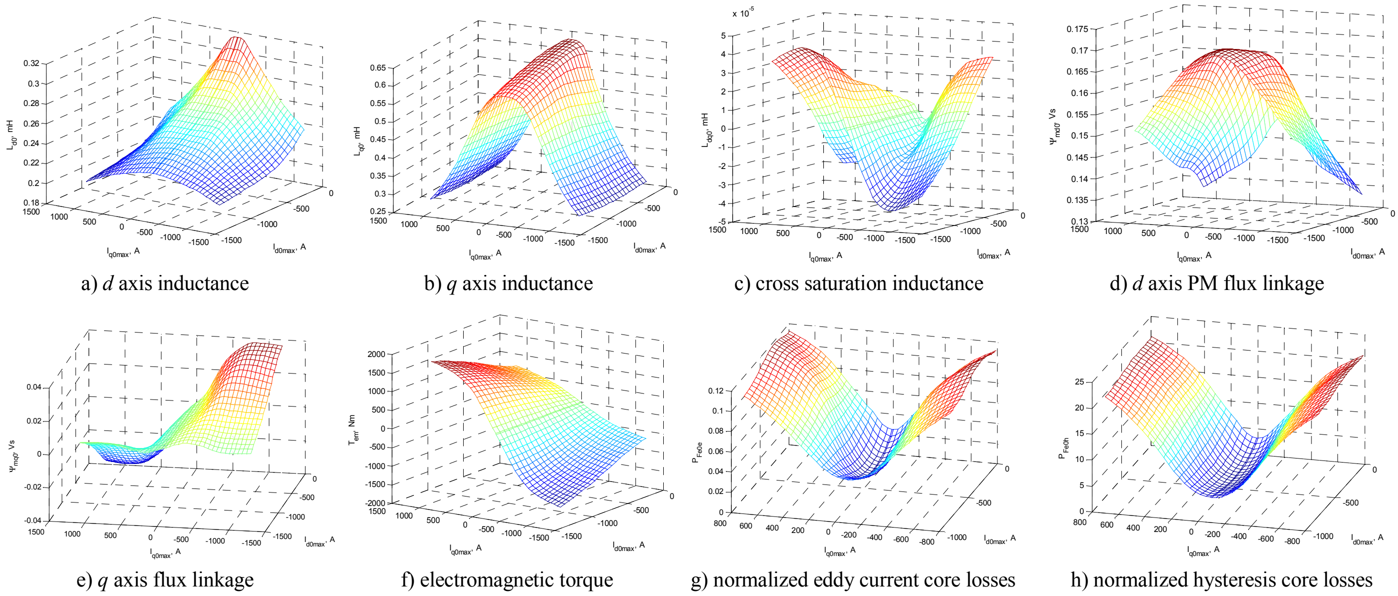

a) d axis inductance; b) q axis inductance; c) cross saturation inductance; d) d axis PM flux linkage; e) q axis flux linkage; f) electromagnetic torque; g) normalized eddy current core losses; h) normalized hysteresis core losses

Fig. 8. 2D maps of IPM motor inductances, PM flux linkages, electromagnetic torque, and normalized core losses

In this case the linear current density on the stator perimeter remains constant. The maps of the scaled motor in Fig. 8 together with the *d-q* currents (I_{dmax}, I_{qmax}), resistance (R) and losses (P_{Cu}) of the armature winding, and windage losses (P_w) of the scaled motor are given by [18]

$$
\begin{aligned}
k_W &= \frac{N_c}{a_p}\frac{a_{p0}}{N_{c0}} \\
T_{em} &= k_R^2 k_A T_{em0} \\
I_{d\max} &= \frac{k_R}{k_W} I_{d0\max} \\
I_{q\max} &= \frac{k_R}{k_W} I_{q0\max} \\
L_d &= k_W^2 (k_A L_{d0co} + k_R L_{ew0}) \\
L_q &= k_W^2 (k_A L_{q0co} + k_R L_{ew0}) \\
L_{dq} &= k_W^2 k_A L_{dq0} \\
L_{qd} &= k_W^2 k_A L_{qd0} \\
\Psi_{md} &= k_W k_R k_A \Psi_{md0} \\
\Psi_{mq} &= k_W k_R k_A \Psi_{mq0} \\
R &= \left(\frac{k_W}{k_R}\right)^2 (k_A R_{0co} + k_R R_{0ew}) \\
P_{Cu} &= k_A P_{Cu0co} + k_R P_{Cu0ew} \\
P_{Feh}^0 &= k_R^2 k_A P_{Fe0h} \\
P_{Fee}^0 &= k_R^2 k_A P_{Fe0e} \\
P_{w(\omega_{m0})} &= k_R^5 P_{w0(\omega_{m0})}
\end{aligned} \tag{24}
$$

where the subscript 0 refers to the referent motor, the subscript *co* refers to the core region, and the subscript *ew* refers to the end winding region. The windage losses are caused by the cooling fan mounted on the motor shaft and for the referent motor they are determined by a 3D computational fluid dynamics (CFD) model [24] at the rated mechanical speed (ω_{m0}) given in Table I. Since the speed of the tram is varying, the windage losses of the scaled motor are expressed as a function of speed using

$$P_{w(\omega_m)} = k_R^5 \left(\frac{\omega_m}{\omega_{m0}}\right)^3 P_{w0(\omega_{m0})} \tag{25}$$

If the average iron and copper losses of the reference motor for the driving cycle are equal to $P_{Fe0}+P_{Cu0}$ and the hot spot temperature in the winding is within the limits defined by the thermal insulation class F, then it can be assumed that the scaled motor will not heat up more than the reference motor if its average copper and iron losses during the same driving cycle are less or equal to the scaled average losses of the reference motor, i.e. if

$$\overline{P}_{Fe} + \overline{P}_{Cu} \le k_R^2 k_A \overline{P}_{Fe0} + k_A \overline{P}_{Cu0co} + k_R \overline{P}_{Cu0ew} \tag{26}$$

This condition is then applied as an inequality constraint in the optimization algorithm. Of course, this constraint is an approximation and it can be replaced with a fast and accurate thermal model of the motor which would provide more reliable data on the winding temperature of the scaled motor.

The model of the motor is implemented by combining (18) and (24) with nonlinear programming (MATLAB function *fmincon*) to obtain the optimal values of I_d and I_q for the torque required by the traction effort curve of the driving cycle at a given speed to yield the MTPA control and to satisfy the DC bus voltage limit in the flux weakening regime.

B. Model of the NPC three-level converter

The two-level topology of the power converter is a standard solution for industrial variable speed drives including traction applications as well. The three-level topology has been exploited mainly in renewable energy sources due to its low price-to-performance ratio, inherently low total harmonic distortion (THD) of the output voltage, and low switching losses. Another favourable feature significant for traction applications is reduced acoustic noise in the audible range.

For optimization purposes, the model of the three-level converter must be computationally efficient which is not possible to achieve by using integration methods for solving a set of differential equations following a standard approach implemented in commercial software like Plexim PLECS, Ansoft Simplorer, Matlab SimPowerSystems, SPICE. An alternative is to use a model averaged within one switching period. The basic setup for this model has been established as presented in [25].

The primary output results of the converter model relevant for the traction drive optimization will be the total losses (conduction+switching) that will be added to the motor loss as one of the objective functions and the temperature rise of the PN junction as the main constraint.

The topology of an NPC three-level inverter is shown in Fig. 9. Each of the three legs consists of four controllable IGBTs and six diodes. Diodes D_{5x} and D_{6x} (x=a,b,c) connect the output leg with the DC link common point. Table II shows the allowed switching states of a single leg. It is apparent that three voltage levels are available which the name of the inverter topology refers to.

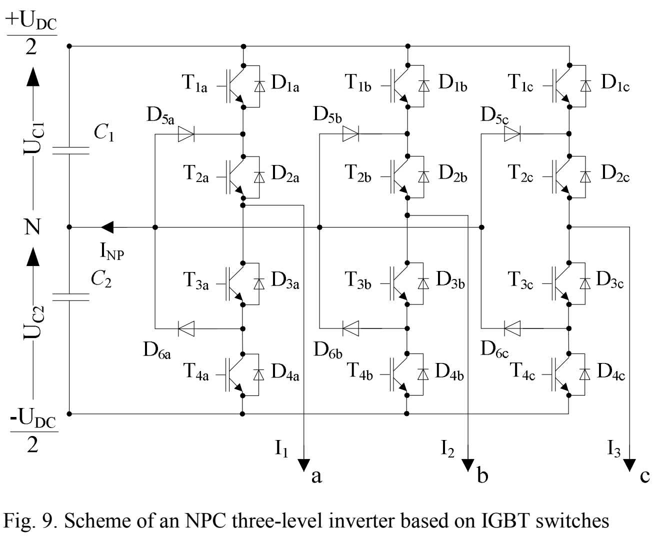

Fig. 9. Scheme of an NPC three-level inverter based on IGBT switches

TABLE II. OUTPUT VOLTAGE STATES OF THE NPC INVERTER

T_{1x}	T_{2x}	T_{3x}	T_{4x}	U_{aN}
1	1	0	0	$+U_{DC}/2$
0	1	1	0	0
0	0	1	1	$-U_{DC}/2$

The averaged model is based on switching functions for each switch in one leg. The switching functions are time dependent functions which can take two values

$$q_x(t) = \begin{cases} 1, & \text{switch in ON} \\ 0, & \text{switch is OFF} \end{cases} \tag{27}$$

In order to define the required number of switching functions, the general model of the three-level inverter clamped to the neutral point defined using ideal switches can be considered as shown in Fig. 10. It is obvious that switching functions $q_1(t)$, $q_{23}(t)$, $q_4(t)$ corresponding to the switches S_1, S_{23} i S_4 can be defined. Since any two switches cannot be turned on at the same time, the following is valid

$$q_1(t) + q_{23}(t) + q_4(t) = 1 \quad \forall t \tag{28}$$

The switching functions can be considered as digital signals which in fact they are, so (28) can be written as

$$q_1(t) + q_4(t) = \overline{q}_{23}(t) \tag{29}$$

where $\overline{q}_{23}(t)$ is the inverse of the function $q_{23}(t)$. Hence there are two independent switching functions $q_1(t)$ and $q_4(t)$ which are obtained by comparing two reference signals with two carrier signals as depicted in Fig. 11. In practical implementation, very often a single carrier signal is used by introducing the amplitude shift of the reference signal based on two switching functions which are natural to three-level topology (Fig. 12). This comparison yields the switching functions shown in Fig. 13.

The voltages and currents of the model in Fig. 10 can now be expressed using

$$\begin{aligned} u_{AN} &= q_1(t) \cdot \frac{U_{DC}}{2} - q_4(t) \cdot \frac{U_{DC}}{2} \\ i_{pA} &= q_1(t) \cdot I_A \\ i_{nA} &= -q_4(t) \cdot I_A \\ i_{npA} &= -q_{23}(t) \cdot I_A = -(1 - q_1(t) - q_4(t)) \cdot I_A \end{aligned} \tag{30}$$

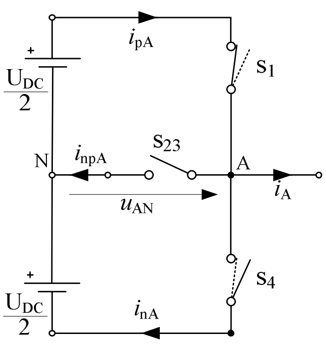

Fig. 10. One phase leg of a general model of an NPC three-level inverter

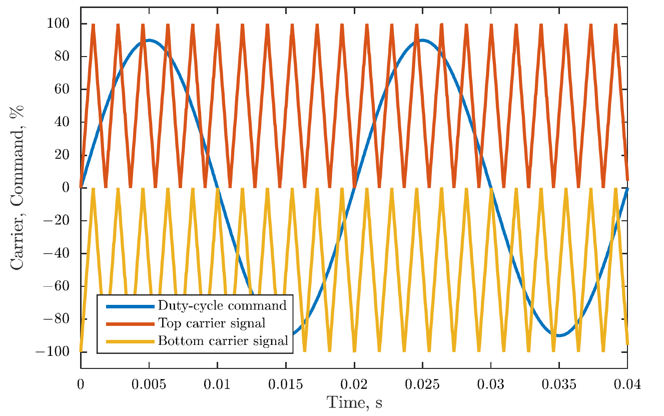

Fig. 11. Basic principle of modulation of an NPC three-level inverter with two carrier signals (natural sinusoidal modulation)

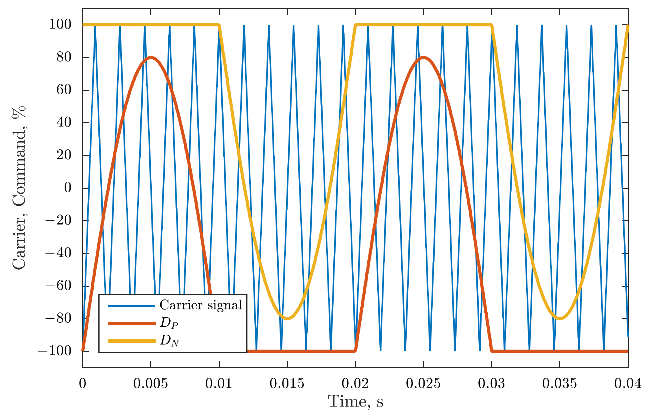

Fig. 12. Modified modulation of an NPC three-level inverter with a single carrier signal (natural modulation)

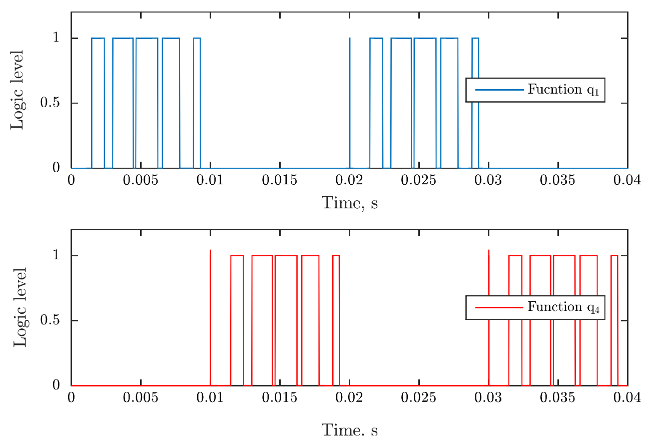

Fig. 13. Switching functions q_1(t) and q_4(t)

If q_1(t) and q_4(t) are averaged within the switching interval $T_{SW}=1/f_{SW}$, where f_{SW} is the switching frequency, the instantaneous averaged switching functions thus obtained are

$$\begin{aligned} \overline{q}_1(t) &= \frac{1}{T_{SW}} \int_{t-T_{SW}}^{t} q_1(t)\mathrm{d}t \equiv D_P \\ \overline{q}_4(t) &= \frac{1}{T_{SW}} \int_{t-T_{SW}}^{t} q_4(t)\mathrm{d}t \equiv D_N \end{aligned} \tag{31}$$

The reference signal is usually defined to be constant during a switching period (regular modulation) which yields the reference signal in Fig. 14. According to (31), in the case of regular modulation the instantaneous averaged switching functions are equal to the reference signals in Fig. 14.

Combining (30) and (31) yields the average values of voltages and currents at the output of the averaged model of an NPC three-level inverter (Fig. 15)

$$\begin{aligned}
&\bar{u}_{AN} = \bar{u}_{C1} \cdot D_{PA} - \bar{u}_{C2} \cdot D_{NA} \\
&\bar{u}_{BN} = \bar{u}_{C1} \cdot D_{PB} - \bar{u}_{C2} \cdot D_{NB} \\
&\bar{u}_{CN} = \bar{u}_{C1} \cdot D_{NA} - \bar{u}_{C2} \cdot D_{NC} \\
&\bar{i}_P = \bar{i}_{pA} + \bar{i}_{pB} + \bar{i}_{pC} = D_{PA}(t) \cdot \bar{i}_A + D_{PB}(t) \cdot \bar{i}_B + D_{PC}(t) \cdot \bar{i}_C \\
&\bar{i}_N = \bar{i}_{nA} + \bar{i}_{nB} + \bar{i}_{nC} = D_{NA}(t) \cdot \bar{i}_A + D_{NB}(t) \cdot \bar{i}_B + D_{NC}(t) \cdot \bar{i}_C \\
&\bar{i}_{NP} = \bar{i}_{npA} + \bar{i}_{npB} + \bar{i}_{npC} = (D_{PA}(t) + D_{NA}(t)) \cdot \bar{i}_A + (D_{PB}(t) + \\
&\qquad D_{NB}(t)) \cdot \bar{i}_B + (D_{PC}(t) + D_{NC}(t)) \cdot \bar{i}_C - \bar{i}_A - \bar{i}_B - \bar{i}_C
\end{aligned} \tag{32}$$

The neutral point of the capacitor is usually not connected to the power source so the inverter control must ensure equal distribution of voltages among capacitors C_1 and C_2. The ripple of the neutral point voltage can be obtained from the average neutral point current

$$\bar{u}_{NP}(t) = \frac{1}{4C_{DC}} \int i_{NP}(t)\,\mathrm{d}t \tag{33}$$

where C_{DC} is the total capacitance of the DC bus. The capacitor voltages are then

$$\begin{aligned}
\bar{u}_{C1} &= \frac{U_{DC}}{2} - \bar{u}_{NP}(t) \\
\bar{u}_{C2} &= \frac{U_{DC}}{2} + \bar{u}_{NP}(t).
\end{aligned} \tag{34}$$

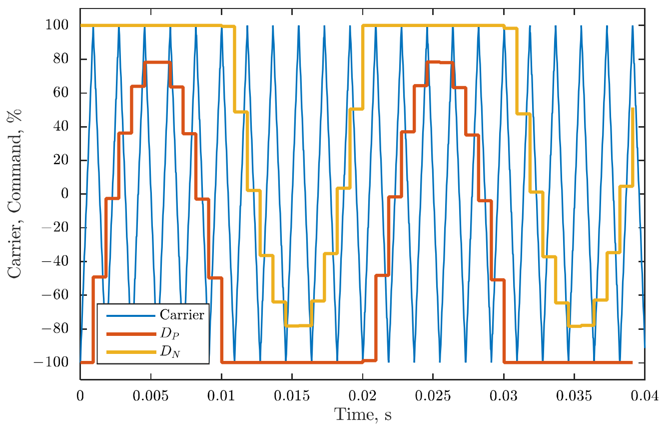

Fig. 14. Modified modulation of an NPC three-level inverter with a single carrier signal and constant reference within the switching period (double update regular modulation)

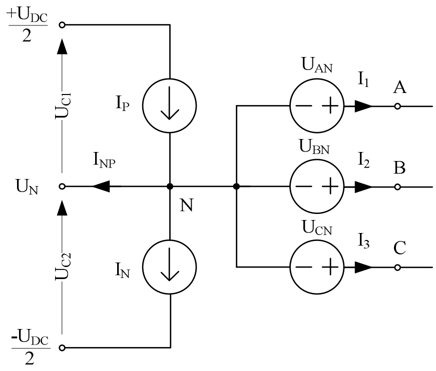

Fig. 15. Averaged model of an NPC three-level inverter

Calculation of the DC bus voltage

The DC bus voltage is important for calculation of switching losses. The dynamic models of the motor and inverter cannot be used for its calculation because they are very time consuming. An alternative approach is used here which utilizes the traction power known from the traction effort curve of the tram with assumed average efficiencies of the drive components. Fig. 16 shows a simplified model of the DC bus which consists of an ideal DC voltage source ($U_s = 600$ V) and an ideal diode connected in series. The diode emulates the rectifier normally present in the tram power supply stations of the city network. The resistance R_{DC}=20 mΩ represents the equivalent resistance of the power supply network.

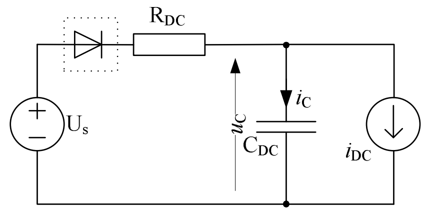

Fig. 16. Simplified model of the DC bus

The DC current i_{DC} fed to the inverter can be expressed using the total electrical power P_{vel} required by the tractive effort of the vehicle

$$i_{DC}(t) = \frac{P_{vel}(\mathrm{t})}{u_c(\mathrm{t})} = \frac{P_{vmech}(t)}{\eta_{mot}\eta_{gear}\eta_{inv}} + P_{aux} \tag{35}$$

where P_{vmech} is the total mechanical power on the wheels (depends on the instantaneous demand of the driving cycle), $P_{\mathrm{aux}} = 40$ kW is the average power required by auxiliary systems (heating, air conditioning, lights…), and $\eta_{\mathrm{mot}} = 0.91$, $\eta_{\mathrm{gear}} = 0.99$, $\eta_{\mathrm{inv}} = 0.97$ are the assumed average efficiencies of the motor, gearbox and inverter respectively. The capacitor current can then be expressed as

$$i_C(t) = \frac{U_S - u_C(\mathrm{t})}{R_{DC}} - \frac{P_{vel}(t)}{u_C(t)} \tag{36}$$

The time derivative of the capacitor voltage is then

$$\frac{\mathrm{d}u_C}{\mathrm{d}t} = \frac{1}{C_{DC}}\left(\frac{U_S - u_C(\mathrm{t})}{R_{DC}} - \frac{P_{vel}(t)}{u_C(t)}\right) \tag{37}$$

The time variations of DC bus voltage and current calculated using the described model for a single driving cycle of the tram are shown in Fig. 17. Five different periods can be distinguished: acceleration with constant maximum torque, acceleration with constant maximum power, driving at constant speed, regenerative braking with constant maximum braking power, regenerative braking with constant maximum braking torque. The DC bus voltage limit during regenerative braking is increased to 750 V which reflects the actual limit for the tram TMK2200.

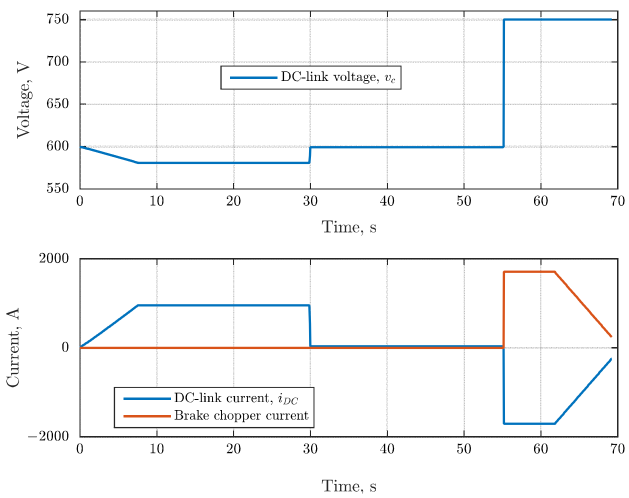

Fig. 17. Simulated DC bus voltage and current in one driving cycle

Current load of the semiconductor switches

The currents in the semiconductor devices (four IGBTs and six diodes per leg) can be determined using previously defined averaged switching functions. Since an IGBT can conduct the current only in one direction (from collector to emitter), the sign of the output current can be used to uniquely determine which switch can conduct. For that reason, the output current is divided into two signals, positive and negative.

If only the first leg in Fig. 9 is considered, then the positive current i_P is conducted by transistors T_{1a}, T_{2a} and diodes D_{3a}, D_{4a}, D_{5a} while the negative current i_N is conducted by transistors T_{3a}, T_{4a} and diodes D_{1a}, D_{2a}, D_{6a}. The switching functions for T_{1a} and T_{4a} are defined by the referent modulation signals D_P and D_N from (31). The transistor T_{2a} is switching in counterphase from T_{4a}, and T_{3a} is in counterphase from T_{1a}.

For calculation of losses using the averaged model it is required to know the average current of the switch $\bar{i}_X$, the peak value of the current $\hat{i}_X$, and the current during period in which the transistor is switching $\tilde{i}_X$. The expressions for calculation of all these current components for individual switches are shown in Table III. The example of currents for switch T_{1a} calculated using this model is shown in Fig. 18.

Calculation of inverter losses

With the known inverter currents and voltages, the losses dissipated on individual power switches can now be calculated. The parameters of the switches used for loss calculations which are available in manufacturers' catalogues are: IGBT voltage drop as a function of current ($U_{ce}=f(I_c)$), IGBT turn-on ($E_{on}=f(I_c)$) and turnf-off ($E_{off}=f(I_c)$) energy, diode voltage drop as a function of current ($U_f=f(I_D)$), and diode reverse recovery energy ($E_{rr}=f(I_D)$). These characteristics are usually provided as graphs and in this case, they are fitted using 4th order polynomial functions.

TABLE III. AVERAGE, PEAK AND SWITCHING CURRENT IN THE SWITCHES OF AN NPC THREE-LEVEL INVERTER

	$\bar{i}_X$	$\hat{i}_X$	$\tilde{i}_X$
T_{1a}	$i_P D_P$	i_P	i_P, if $0<D_P<1$ 0, if $D_P=0 \vee D_P>1$
T_{2a}	$i_P(1-D_N)$	i_P	i_P, if $0<D_N<1$ 0, if $D_N=0 \vee D_N>1$
D_{3a}	$i_P D_N$	i_P	0, soft switching
D_{4a}	$i_P D_N$	i_P	i_P, if $0<D_P<1$ 0, if $D_P=0 \vee D_P>1$
D_{5a}	$i_P(1-D_P-D_N)$	i_P	i_P, if $0<D_P<1$ 0, if $D_P=0 \vee D_P>1$
T_{4a}	$i_N D_N$	i_N	i_N, if $0<D_N<1$ 0, if $D_N=0 \vee D_N>1$
T_{3a}	$i_N(1-D_P)$	i_N	i_N, if $0<D_P<1$ 0, if $D_P=0 \vee D_P>1$
D_{2a}	$i_N D_P$	i_N	0, soft switching
D_{1a}	$i_N D_P$	i_N	i_N, if $0<D_P<1$ 0, if $D_P=0 \vee D_P>1$
D_{6a}	$i_N(1-D_P-D_N)$	i_N	i_N, if $0<D_N<1$ 0, if $D_N=0 \vee D_N>1$

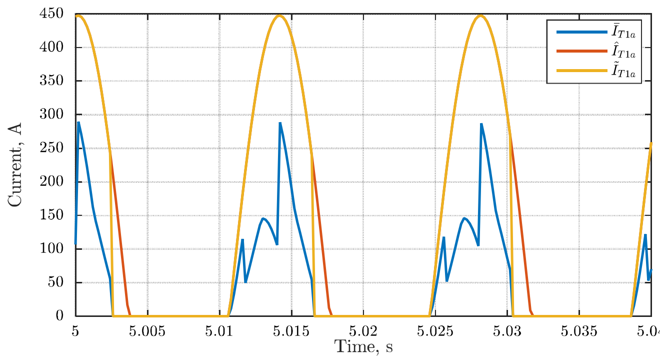

Fig. 18. Current components of the switch T_{1a} calculated using the averaged model of an NPC three-level inverter

If it is assumed that the output current during a switching period is constant and equal $\hat{i}_x$ and the duty cycle of the observed switch x equals D_P, the conduction losses can be calculated as

$$P_{condx} = U_{ce}\left(\hat{i}_x\right)\hat{i}_x D_p \equiv U_{ce}\left(\hat{i}_x\right)\bar{i}_x \qquad (38)$$

where $\hat{i}_x$ is the average current as defined in Table III. It can be noticed that conduction losses are not a function of duty cycle if previously calculated average current exists. The same approach is used to calculate the conduction losses of a diode.

The switching losses are calculated from the switching energies obtained from polynomial fits and the currents $\tilde{i}_X$ calculated according to Table III

$$P_{swTx} = \begin{cases} \dfrac{E_{on}\left(\tilde{i}_x\right) + E_{off}\left(\tilde{i}_x\right)}{T_{sw}} \cdot \dfrac{u_{ce}}{U_{dat}}, & \forall t \text{ where } \tilde{i}_x(t) > 0 \\ 0, & \forall t \text{ where } \tilde{i}_x(t) \le 0 \end{cases}$$
$$P_{swDx} = \begin{cases} \dfrac{E_{rr}\left(\tilde{i}_x\right)}{T_{sw}} \cdot \dfrac{u_{ce}}{U_{dat}}, & \forall t \text{ where } \tilde{i}_x(t) > 0 \\ 0, & \forall t \text{ where } \tilde{i}_x(t) \le 0 \end{cases} \tag{39}$$

The example of switching losses of the transistor T_{1a} calculated using the described model are shown in Fig. 19. The total power losses can be expressed as a sum of conduction and switching losses in all semiconductor devices of the inverter, which for the case of a three-phase NPC three-level inverter equals

$$P_{loss} = \sum_{i=1}^{4} \sum_{j=a,b,c} \left(P_{condT_{ij}} + P_{swT_{ij}}\right) + \sum_{i=1}^{6} \sum_{j=a,b,c} \left(P_{condD_{ij}} + P_{swD_{ij}}\right) \tag{40}$$

where i is the number of the phase and j is the number of a particular device in that phase. The inverter losses calculated for the duration of a single driving cycle are shown in Fig. 20.

Thermal model of the inverter

The losses in the devices will cause the temperature rise of the PN junction which must be kept below the maximum allowed value. For calculation of the temperature rise a well-established thermal model has been used [26]. For simplification, one dimensional heat flow has been considered with an assumption of fixed temperature of the heat sink. The manufactures of the devices usually provide the plot of the transient thermal impedance as a function of time in their catalogues. The thermal impedance can be fitted using higher order transfer function obtained from the equivalent circuit (Fig. 21) whose parameters are determined using some optimization method to get the same response as the one in the catalogue. The results of the thermal model applied to the NPC three-level inverter of the tram are shown in Figs. 22 and 23.

The junction temperature is used as one of the constraints in the optimization process.

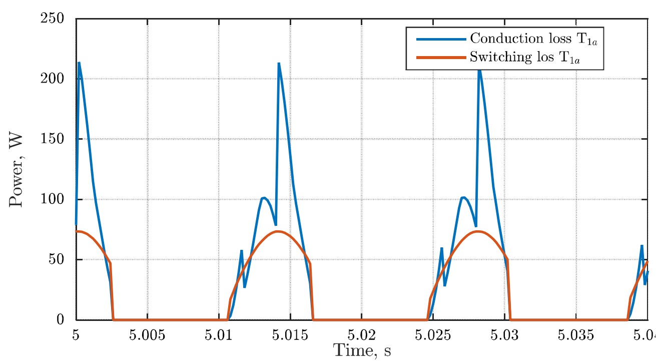

Fig. 19. Power dissipation on the switch T_{1a} caused by conduction and switching losses

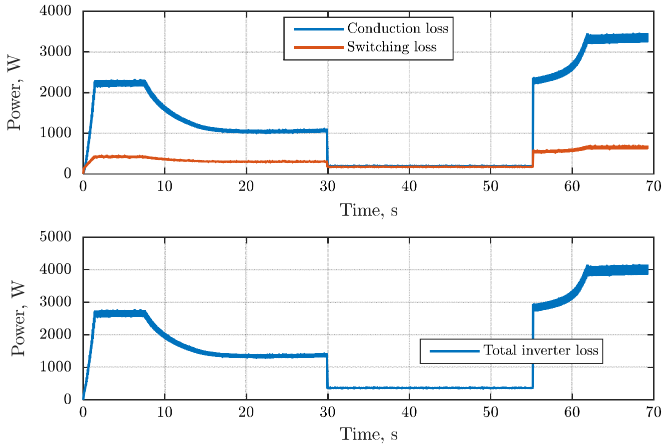

Fig. 20. Switching, conduction and total losses of the NPC three-level inverter developed during a single driving cycle of the tram

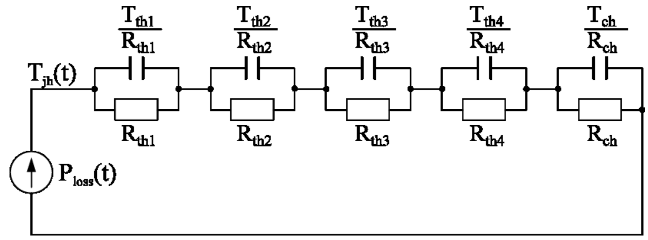

Fig. 21. Model of the transient thermal impedance

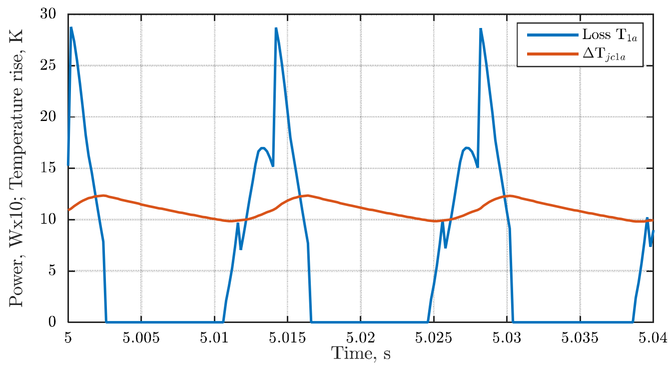

Fig. 22. Detail from the results of the thermal model: losses and junction temperature of the transistor T_{1a}

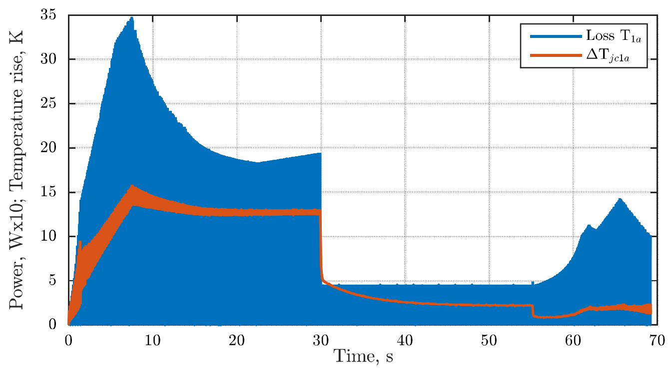

Fig. 23. Losses and junction temperature of the transistor T_{1a} developed during a single driving cycle of the tram

C. Results of multiobjective optimization of the traction drive system for the KONČAR TMK2200 low-floor tram

The software implementation of the tram drive multiobjective optimization is visualized in Fig. 24. The optimization code consists of four main parts:

1. Kinematic model of the vehicle which determines the required torque and motor speed as a function of time,
2. Computationally efficient mathematical models of drive components (motor and inverter),
3. Subprogram for connecting component models to a single functional unit,
4. Programming code for multiobjective optimization.

Considering the vehicle dynamics and the coupled models of the traction motor and the NPC three-level converter which are used to model the traction drive system as a whole, the parameters of the optimization problem have been defined as listed in Table IV. The optimization is performed using *mixed integer distributed ant colony optimization* (MIDACO) [27].

Two driving profiles have been analyzed. Profile 1 is the standard driving cycle of the tram TMK2200 and Profile 2 is the cycle with reduced tractive effort. The parameters which define the tractive effort for both profiles are listed in Table V. The required motor torque and speed as a function of time for both profiles are shown in Figs. 25 and 26. The optimization results are displayed in Figs. 27 to 33. All calculation were performed using a PC with Intel i7-6700K@4.2GHz processor with 64GB DDR4 RAM. The stopping criterion for both profiles was 10000 objective function evaluations.

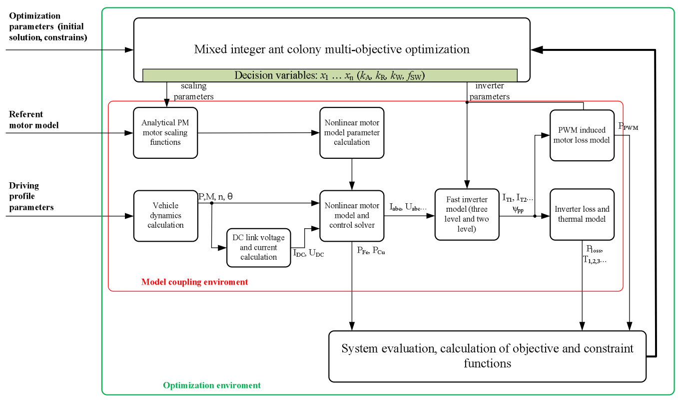

Fig. 24. Block scheme of the software for traction drive optimization

TABLE IV. OBJECTIVES AND CONSTRAINTS OF THE TRAM DRIVE OPTIMIZATION PROBLEM

Objective functions	Normalized volume of the traction motor ($k_R^2 k_A$)
	Average losses of the motor and inverter in a single standard driving cycle (P_{avg})
Inequality constraints	Average motor losses per driving cycle smaller than scaled losses of the referent motor $P_{mot} \le k_R^2 k_A P_{Fe0} + k_A P_{CuSlot0} + k_R P_{CuEW0}$
	Temperature rise of the PN junction ($T_{JCmax} \le 45$ K)
Optimization variables	Motor scaling factor in the radial direction (k_R) – continuous variable
	Motor scaling factor in the axial direction (k_A) – continuous variable
	Motor rewinding factor (k_W) – discrete variable
	Inverter switching frequency (f_{SW}) - continuous variable

TABLE V. PARAMETERS FOR DEFINITION OF THE TRACTIVE EFFORT

Parameter	Profile 1	Profile 2
Maximum power for acceleration	485 kW	345 kW
Maximum power for regenerative braking	1120 kW	540 kW
Maximum acceleration	1 m/s^2	1 m/s^2
Maximum deceleration	1,4 m/s^2	1,3 m/s^2
Mass of the empty vehicle	42 t	34 t
Mass of the passengers	19,2 t	15,4 t
Maximum speed	70 km/h	60 km/h
Total driving cycle distance	1000 m	1000 m
Number of traction motors	4	4

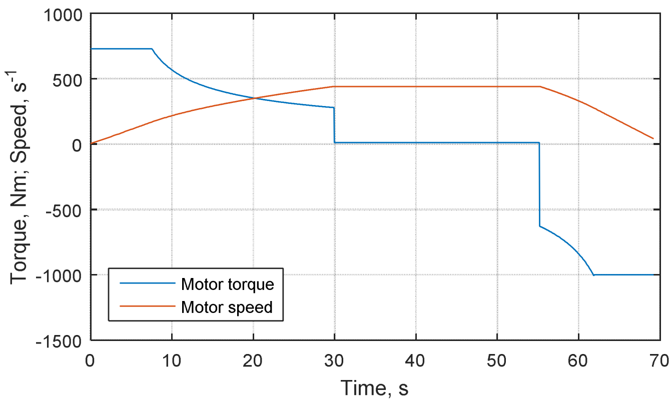

Fig. 25. Standard driving profile of the tram TMK2200 (Profile 1)

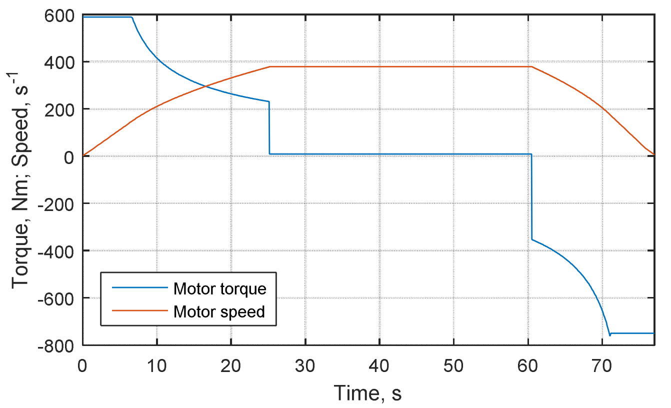

Fig. 26. Driving profile of the tram TMK2200 with reduced tractive effort (Profile 2)

Selection of the radial scaling factor k_R

The radial scaling factor k_R scales all dimensions of the referent motor cross section in the radial direction. In the case of Profile 1 the boundaries are $0.7 \le k_R \le 1.5$ and in the case of Profile 2 $0.4 \le k_R \le 1.2$. It can be noticed in Fig. 27 that optimization in both cases forces the increase in motor size for the purpose of reducing the average cycle losses. In Profile 1 a small set of solutions was found where $k_R < 1$ at the expense of increased losses. The referent motor was optimized for maximum torque density considering Profile 1, but without considering the inverter. In a combined model of the motor and inverter the results indicate that a smaller motor can be built within the constraints of the optimization problem definition.

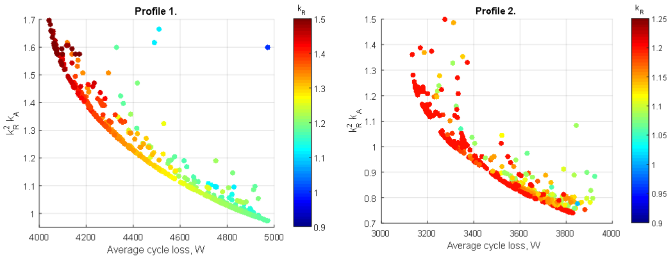

Fig. 27. Radial scaling factor displayed in the objective function space (left Profile 1, right Profile2)

Selection of the axial scaling factor k_A

The axial scaling factor alters the axial length of the laminations stack. In the case of Profile 1 the boundaries are $0.7 \leq k_A \leq 1.6$ and in the case of Profile 2 $0.4 \leq k_A \leq 1.2$. Fig. 28 shows that optimization is pushing the k_A factor towards lower boundary, especially for higher values of the average cycle losses.

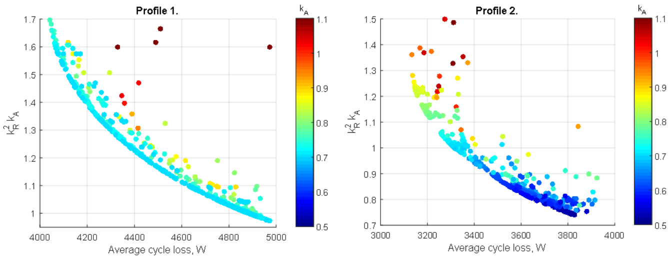

Fig. 28. Axial scaling factor displayed in the objective function space (left Profile 1, right Profile2)

Selection of the rewinding factor k_W

The rewinding factor k_W defines the ratio of the number of turns per coil N_c and the number of parallel paths a_p and thus defines the voltage level required for some motor size and load. Since N_c and a_p can have only discrete values, the factor k_w is also define as discrete variable with a predefined set of values. The following set is used k_W = {1.0, 1.25, 1.5, 1.75, 2.0, 2.25, 2.5, 3.0, 3.5, 4.0, 4.5]. It can be noticed from Fig. 29 that the optimal k_W for Profile 1 equals 2 for all members of the Pareto set, while the choice of k_W in the case of Profile 2 is not unique. The motors with the smallest volume on the Pareto fronts are wound with a factor of 3 up to a normalized volume of 0.9. After that, the motors are wound with a factor of 2.5 up to the volume of 1.1 after which the rewinding factor of 2.25 is used.

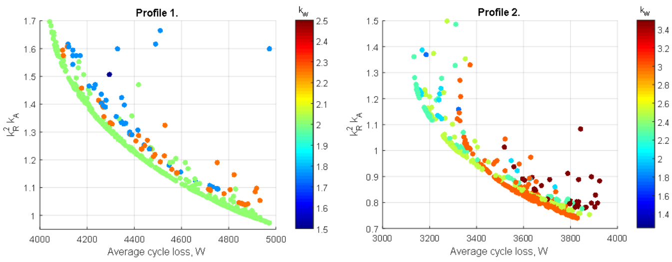

Fig. 29. Rewinding factor displayed in the objective function space (left Profile 1, right Profile2)

Motor losses

The motor losses are shown in Fig. 30. As expected, the motor losses are reduced as the motor volume increases.

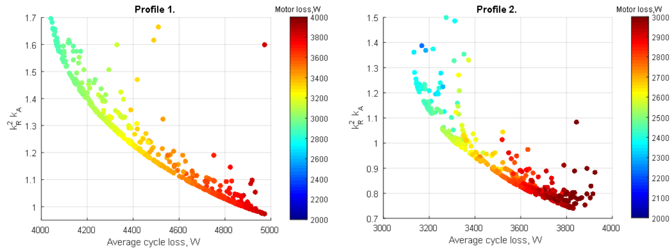

Fig. 30. Motor losses displayed in the objective function space (left Profile 1, right Profile2)

Selection of the switching frequency

The switching frequency is varied as a continuous variable within the boundaries 1.5 kHz$\leq f_{SW} \leq$4.0 kHz. Fig. 31 shows that in the case of Profile 2 the optimization increases the switching frequency as the volume of the motor is reduced. In addition, the sudden changes of the switching frequency can be observed which are related to the changes of the rewinding factor.

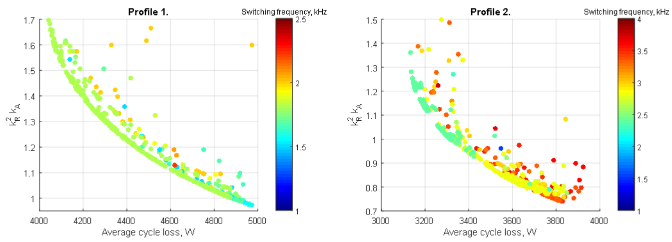

Fig. 31. Switching frequency displayed in the objective function space (left Profile 1, right Profile2)

For some volume of the motor, higher switching frequency reduces the PWM induced losses in the motor, but at the same time increases the switching losses in the inverter. There is a trade-off between these two trends which resulted in the distribution of switching frequencies as shown in Fig. 31. The optimization always aims to minimize the average cycle losses for some volume of the motor or minimize the motor volume for some value of losses. The variation of switching frequency also affects the total averaged inverter losses and the maximum achieved PN junction temperature which is illustrated in Figs. 32 and 33.

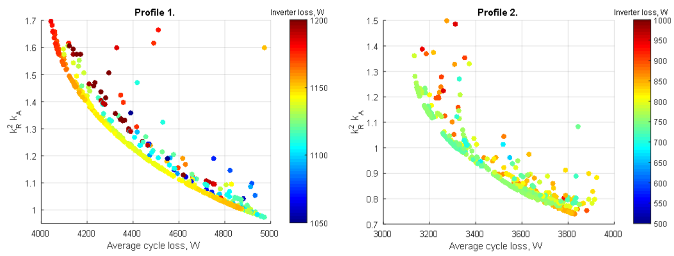

Fig. 32. Averaged losses of the inverter displayed in the objective function space (left Profile 1, right Profile2)

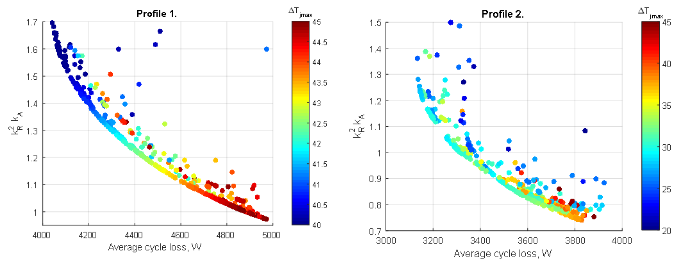

Fig. 33. Maximum temperature rise of the PN junction displayed in the objective function space (left Profile 1, right Profile2)

V. Conclusion

This paper illustrates the basic aspects of optimized design of electric drives for traction applications. The main steps in this process are explained in detail which include modelling of the vehicle dynamics, consideration of the motor and power converter size and ratings, selection of the design variables, definition of the optimization problems (objective functions, variables, constraints), selection of the optimization method, and interpretation of the final results.

The traction drive optimization is by nature a mixed integer nonlinear programming type of multiobjective design problem. The main competing objectives are the size (and therefore the cost) of the drive components (motor and inverter) and the total energy consumption in a predefined driving cycle. The minimization of both cannot be achieved at the same time so multiobjective optimization provides an insight into design trade-offs between these two objectives to facilitate the final design choice. One of the methods for selecting the optimal solution can be to calculate the total life cycle cost of the vehicle by adding the initial cost of the drive and the cost of energy consumption during the lifetime of the vehicle for every optimal solution on the Pareto front and choose the one with the minimum life cycle cost.

The optimization process requires computationally efficient and accurate models of the drive components. Two examples of such models have been presented: scalable saturated model of the IPM motor based on mapped values of inductances, flux linkages and core losses obtained from FEM simulations, and the averaged model of the NPC three-level inverter.

The described optimization principle is illustrated on an example of multiobjective Pareto optimization of a low floor tram using mixed integer distributed ant colony optimization.

Acknowledgment

This work was supported in part by the Croatian Science Foundation under the Project IP-11-2013-7801 Advanced Electric Drives for Traction Applications.

References

[1] M. Ehsani, Y. Gao, and A. Emadi, Modern Electric, Hybrid electric, and Fuel Cell Vehicles: Fundamentals, Theory, and Design, 2nd ed. CRC Press, 2010

[2] Code of Federal Regulations, Energy, 10, parts 400 to 499. Office of the Federal Register National Archives and Records Administration, U.S Government Printing Office, Washington, 1996

[3] A. Steimel, Electric Traction – Motive Power and Energy Supply: Basic and Practical Experience. Oldenbourg Industrieverlag München, 2008

[4] T. D. Gillespie, Fundamentals of Vehicle Dynamics. Society of Automotive Engineers, Inc., Warrendale, PA, 1992.

[5] L. Buhrkall, "Traction System Case Study," IET Professional Development course on Electric Traction Systems, pp. 45-63, 3-7 Nov. 2008, Manchester, UK

[6] S. Stipetić, D. Žarko, and M. Kovačić, "Optimised Design of Permanent Magnet Assisted Synchronous Reluctance Motor Series Using Combined Analytical–Finite Element Analysis Based Approach. " IET Electric Power Applications, Vol. 10, Iss. 5; pp. 330-338, 2016

[7] M. Martinović, D. Žarko, S. Stipetić, T. Jerčić, M. Kovačić, Z. Hanić, and D. Staton, "Influence of Winding Design on Thermal Dynamics of Permanent Magnet Traction Motor," International Symposium on Power Electronics, Electrical Drives, Automation and Motion (SPEEDAM), pp. 397–402., Ischia, Italy, 18 - 20 Jun 2014

[8] T. Gilmore, and R. G. Sladky, "Ratings of Semiconductors for AC Drives," IEEE Transactions on Industry Applications, Vol. 37, No. 2, pp. 434-441, March/April 2001

[9] Voltage Classes for Electric Mobility. German Electrical and Electronic Manufacturers‘ Association, December 2013

[10] D. Žarko, D. Ban, and T. A. Lipo, "Analytical Calculation of Magnetic Field Distribution in the Slotted Air Gap of a Surface Permanent-Magnet Motor Using Complex Relative Air-Gap Permeance," IEEE Transactions on Magnetics, Vol. 42, No. 7, pp. 1828–1837, 2006.

[11] A. Hanić, D. Žarko, and Z. Hanić, "A Novel Method for No-Load Magnetic Field Analysis of Saturated Surface Permanent-Magnet Machines Using Conformal Mapping and Magnetic Equivalent Circuits," IEEE Transactions on Energy Conversion. Vol. 31, No. 2, pp.740-749, 2016

[12] B. L. J. Gysen, K. J. Meessen, J. J. H. Paulides, and E. A. Lomonova, "General Formulation of the Electromagnetic Field Distribution in Machines and Devices Using Fourier Analysis," IEEE Transactions on Magnetics, Vol. 46, No. 1, pp. 39–52, Jan 2010.

[13] Z.Q. Zhu, L.J. Wu, and Z.P. Xia, "An accurate subdomain model for magnetic field computation in slotted surface-mounted permanent-magnet machines', IEEE Transactions on Magnetics, Vol. 46, No. 4, pp. 1100–1115, 2010

[14] R. L. J. Sprangers, J. J. H. Paulides, B. L. J. Gysen, and E. A. Lomonova, "Magnetic Saturation in Semianalytical Harmonic Modeling for Electric Machine Analysis," IEEE Transactions on Magnetics, Vol. 52, No. 2, pp. 1-10, February 2016

[15] D. W. Kemmetmüller, and A. Kugi, "Magnetic Equivalent Circuit Modeling of a Saturated Surface-Mounted Permanent Magnet Synchronous Machine," IFAC-PapersOnLine, Vol. 48, Issue 1, pp. 360-365, 2015

[16] Han-Kyeol Yeo, Dong-Kuk Lim, Dong-Kyun Woo, Jong-Suk Ro, and Hyun-Kyo Jung, "Magnetic Equivalent Circuit Model Considering Overhang Structure of a Surface-Mounted Permanent-Magnet Motor," IEEE Transactions on Magnetics, Vol. 51, No. 3, pp. 1-4, March 2015

[17] J. Goss, P. Mellor, R. Wrobel, D. Staton, and M. Popescu, "The Design of AC Permanent Magnet Motors for Electric Vehicles: A Computationally Efficient Model of The Operational Envelope," 6th International Conference on Power Electronics, Machines & Drives (PEMD 2012), pp. 1–6., 27-29 March 2012, Bristol, UK

[18] S. Stipetić, D. Žarko, and M. Popescu, "Ultra-fast axial and radial scaling of synchronous permanent magnet machines," IET Electric Power Applications, Vol. 10, No. 7, pp. 658–666, 2016.

[19] X. Chen, J. Wang, B. Sen, P. Lazari, and T. Sun, "A High-Fidelity and Computationally Efficient Model for Interior Permanent-Magnet Machines Considering the Magnetic Saturation, Spatial Harmonics, and Iron Loss Effect," IEEE Transactions on Industrial Electronics, Vol. 62, Issue 7, pp. 4044 – 4055, July 2015

[20] C.A.C. Coello and R. L. Becerra, "Evolutionary Multiobjective Optimization Using a Cultural Algorithm," Proceedings of the 2003 IEEE Swarm Intelligence Symposium, pp. 6-13, April 2003.

[21] J. Lee and Sven Leyffer, Mixed integer nonlinear programming. Springer Science & Business Media, 2011.

[22] D. Žarko, S. Stipetić, M. Martinović, M. Kovačić, T. Jerčić, Z. Hanić, "Reduction of Computational Efforts in Finite Element Based

Permanent Magnet Traction Motor Optimization," IEEE Transactions on Industrial Electronics, Vol. PP, Issue 99 (in press), 2017

[23] N. Bianchi and S. Bolognani, "Magnetic Models of Saturated Interior Permanent Magnet Motors Based on Finite Element Analysis," Conference record of Thirty-Third IAS Annual Meeting, pp. 27–34, St. Louis, MO, USA, 12-15 Oct. 1998

[24] T. Jerčić, D. Žarko, M. Martinović, M. Kovačić, J. Jurić, Z. Hanić, and S. Stipetić, "Centrifugal Fan Design for Permanent Magnet Synchronous Motor in a Traction Application, "IEEE International Electric Machines and Drives Conference (IEMDC), pp. 1-7, Miami, FL, USA, 21-24 May 2017

[25] M. Kovačić, I. Mrčela, V. Šunde, and Ž. Jakopović, "Usage of a three-level neutral-point clamped inverter in electric traction applications," Proceedings of the 7th International Conference on Electrical Drives and Power Electronics (EDPE 2013), pp. 278-286, Dubrovnik, Croatia, 2-4 October 2013

[26] V. Blasko, R. Lukaszewski, and R. Sladky. "On line thermal model and thermal management strategy of a three-phase voltage source inverter," Conference Record of the Thirty-Fourth IAS Annual Meeting Vol. 2. pp. 1423 – 1431, Phoenix, AZ, USA, 3-7 Oct. 1999

[27] M. Schlüter, J.A. Egea, and J. R. Banga. "Extended Ant Colony Optimization for Non-Convex Mixed Integer Nonlinear Programming," Computers & Operations Research, Vol.36, Issues 7, pp. 2217-2229, 2009